



Process Control and Characterization of NiCr Coatings by HVOF-DJ2700 System: A Process Map Approach

Alfredo Valarezo, Wanhuk B. Choi, Weiguang Chi, Andrew Gouldstone, and Sanjay Sampath

(Submitted June 23, 2009; in revised form January 13, 2010)

The concept of ‘process maps’ has been utilized to study the fundamentals of process-structure-property relationships in high velocity oxygen fuel (HVOF) sprayed coatings. Ni-20%Cr was chosen as a representative material for metallic alloys. In this paper, integrated experiments including diagnostic studies, splat collection, coating deposition, and property characterization were carried out in an effort to investigate the effects of fuel gas chemistry (fuel/oxygen ratio), total gas flow, and energy input on particle states: particle temperature (T) and velocity (V), coating formation dynamics, and properties. Coatings were deposited on an in situ curvature sensor to study residual stress evolution. The results were reconciled within the framework of process maps linking torch parameters with particle states (1st order map) and relating particle state with deposit properties (2nd order map). A strong influence of particle velocity on induced compressive stresses through peening effect is discussed. The complete tracking of the coating buildup history including particle state, residual stress evolution and deposition temperature, in addition to single splat analysis, allows the interpretation of resultant coating microstructures and properties and enables coating design with desired properties.

Keywords HVOF, mechanical properties, NiCr, process control, process maps, residual stress, transport properties

1. Introduction

High velocity oxy fuel (HVOF) thermal spray is a widely used coating deposition process particularly for metallic alloys and cermets. HVOF consists of a combustion flame of about 3000 K and gases accelerated to about 1000 m/s. Particles are injected internally within the nozzle either axially or radially to the flame, melted (or thermally softened) and accelerated towards a substrate where they deposit to built-up through successive particle impingement. The compaction resultant from the high-velocity impact results in dense coatings with excellent adhesion. The actual formation of the coatings particle by particle involves multiple physical-chemical interactions between materials and gases and between the droplets and substrate.

Comprehensive and integrated efforts are underway around the world to advance in the understanding of these complex process-material interactions with a goal to (i) tailor the properties of coatings to meet stringent design criteria and performance and (ii) narrow the

variability of hardware operation and supplies (powder, gases) on the reliability, and consistency in production of coatings.

In this paper, a systematic study of the process-microstructure-property relationship is presented in the framework of process maps for HVOF process. These scientifically developed and illustrated maps are intended not only to be a reference material for coating designers who seek targeted property values but also a methodology for process optimization.

A guide to explore the operational process domain is suggested based on particle state (temperature, T , and velocity, V) measurements. Variation of volume flow of gases (oxygen, fuel, and air) derived into a consistent method to explore the T-V diagram. The usage of other fuel chemistries or nozzle designs that change significantly the particle state may be explored under a similar procedure. Coatings were sprayed at selected conditions to study the nature of coating build-up and property variability. Although several authors have attempted analogous exploration (Ref 1-6) of the HVOF thermal spray processes, the presented strategy is unique in that it connects process variables to multiple design relevant properties and integrates the various subsets of process manipulation into a unifying mapping theme.

Ni-20%Cr (wt.%) in solid solution was chosen as the representative material for this study. In addition to being representative of typical powder compositions used in production of HVOF thermal spray (i.e. CoNiCrAlYs, T-800 (CoCrMo), etc), the system offers simultaneously simplicity in characterization while capturing many of the important process effects on microstructure including preferential oxidation of its components (Ref 7), residual

Alfredo Valarezo, Wanhuk B. Choi, Weiguang Chi, Andrew Gouldstone, and Sanjay Sampath, Materials Science and Engineering, Stony Brook University, Stony Brook, NY. Contact e-mail: avalarezo@notes.cc.sunysb.edu.

stresses and heterogeneous microstructural features. Knowledge of bulk property values of NiCr also enables benchmarking the process derived variation in coating properties and connects to the contributing microstructural attributes. HVOF coatings of Ni-20%Cr material are used in hot corrosion applications for boilers (Ref 8) owing to the low porosity, fine grain size and lamellar structure. During service, there exists formation of oxides in splat boundaries and open pores due to penetration of oxidizing species. Oxides protect splat material and parent substrate material from further oxidation. These evidences suggest that oxidation levels and intersplat/interpass bonding between splat-splat, which is part of this study, will make the coatings perform in different ways. An example of such effects is reported by Tang et al. (Ref 9) studying TGO growth in CoNiCrAlY-HVOF coatings under various process conditions.

A hybrid Diamond Jet (DJ) gun with a convergent-divergent nozzle from Sulzer Metco (Westbury, NY) was used in this study. Particle state was monitored by two-wavelength pyrometry principle (Accuraspray sensor from Tecnar, Quebec, Canada) and several properties (i.e. thermal conductivity, elastic modulus, hardness, etc.) were concurrently measured in the deposited coatings. The peening intensity of the impacting particles was monitored during spraying through an in situ curvature measurement approach (Ref 10), and correlated to the microstructure, splats, residual stress and hardness of the deposits.

2. Process Maps

Due to the high number of complexities and stochastic events during the deposition of thermal spray coatings, there is a need of a process science approach to link the

process control to the applications by means of a detailed understanding of the particle state, deposition and properties of the coatings. Typical approaches generally optimize the number of operational variables in a Design-of-Experiments matrix in order to enhance the performance of a coating in an application. Afterwards, properties of the optimum coating are evaluated and specified for the application. These methods, although efficient, bring up very limited understanding in the commonalities of processing of different materials; where in contrast, process maps do so.

A *Process Map*, schematically described in Fig. 1, in thermal spray can be described as a series of systematic relationships connecting the process variables to the energetic particle state (kinetic, thermal), *first order process map*, and subsequently, connecting the particle state to relevant properties of coatings (obtained both in situ and ex situ). Ultimately, this allows coating designers to choose a desired combination of properties and correlate them to a particle state, and follow back through the sequence of such maps until defining the process parameters for coating deposition.

Over the last decade researchers have vigorously pursued the development and implementation of process maps. A number of examples have been reported in the literature for air plasma spraying of Mo (Ref 11) and YSZ (Ref 12, 13), and for HVOF spraying of dense alumina coatings (Ref 4), etc. These studies highlight that melting state and kinetic energy of the particles and local deposition temperature (driven by torch heat input or particle deposition temperature-controlling deposition rates) are likely the most important factors controlling the microstructure and properties of the coatings.

Considering the aforementioned benefits of *Process Maps*, this methodology is adopted in this study to achieve optimization in process control and coating properties.

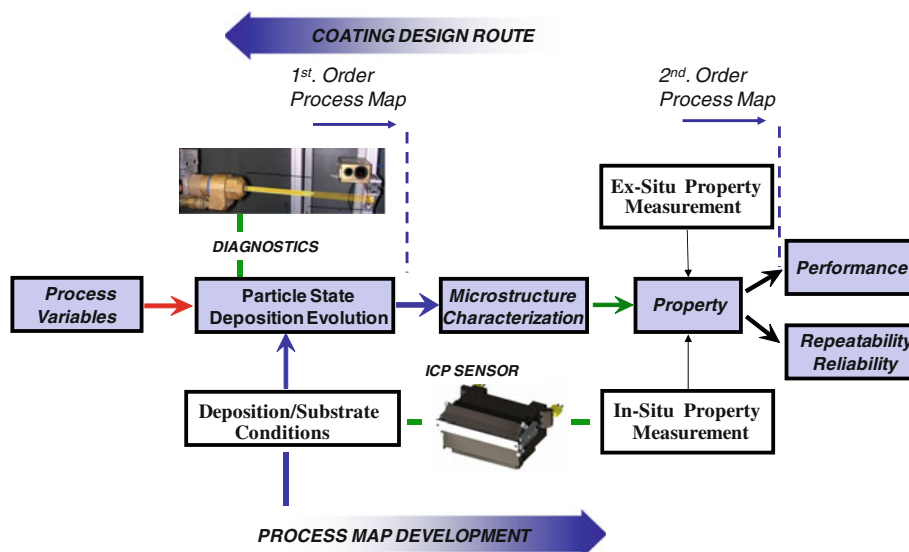


Fig. 1 Overview of process maps methodology

3. Experimental Methods

3.1 First-Order Process Maps: Design of Experiments

The operating space of a spraying gun can be explored by tuning the flow of gases (for plasma spraying, amperage is also considered as a variable). Thus, in plasma spraying, two gases plus current make three operating parameters and therefore three variables in the design of experiments, that is to say: total volume flow, ratio of primary/secondary gases and current. In HVOF, two operating gases define two variables: total volume flow of gases and the ratio between them. Examples of this treatment of variables can be found elsewhere (Ref 4, 11, 12).

The DJ-HVOF system used in this study provides three independent operational parameters: oxygen, fuel, and air flow. The operating space in this study was explored by tuning two of them: oxygen volume flow and fuel volume flow. Air volume flow was kept constant in each set of experiments (two values: 351 and 316 lpm), since its participation in the combustion is not clear. It is generally recognized that the oxygen content of the air may not be fully participating in the combustion reaction provided that the air is fed in the outer rim close to the nozzle wall. Nevertheless, in this paper the full amount of oxygen from the air is considered in the calculations, similar to Ref 14. On the other hand, the nitrogen content of the air is considered to be cooling the flame and the nozzle, as well as contributing to the momentum of the particles (Ref 14). Spraying parameters are described in Table 1.

The flame energy was computed from the heat input of the combustion of the fuel exerting a corresponding factor due to the stoichiometry of the reaction. Thus, fuel/oxygen

ratio, γ was calculated including the 21 vol.% of oxygen in the air supply, as follows:

$$\gamma = \frac{\text{Fuel flow}}{(\text{Oxygen flow} + 0.21 * \text{air flow})} \quad (\text{Eq 1})$$

The stoichiometric ratio for the combustion of propylene fuel C_3H_6 in an HVOF gun is 0.23 from the reaction equation: $1 \text{ C}_3\text{H}_6 + 4.307 \text{ O}_2 \rightarrow 1.903 \text{ CO} + 1.097 \text{ CO}_2 + 0.382 \text{ H} + 0.432 \text{ H}_2 + 2.004 \text{ H}_2\text{O} + 0.388 \text{ O} + 0.745 \text{ OH} + 0.698 \text{ O}_2$ (Ref 15). Energy input E shown in Table 1 was computed according to:

$$E = v * \frac{\gamma_{\text{stoich}}}{\gamma} * \Delta H_c \quad (\text{Eq 2})$$

where v is the flow rate of fuel, γ is the ratio of fuel to oxygen, γ_{stoich} is the stoichiometric ratio, and ΔH_c is the heat of combustion of the fuel per liter (propylene $\text{C}_3\text{H}_6 = 82 \text{ KJ/L}$ (Ref 16)). The fraction $\gamma_{\text{stoich}}/\gamma$ represents the portion of fuel burned with the oxygen. If the flame is either oxygen rich or stoichiometric, the fraction is taken equal to the unity provided that all the fuel is consumed.

Two sets of experiments were conducted at different total volume flow (summation of fuel, oxygen, air, and carrier gas flow): ~620 lpm and ~600 lpm, and varying the stoichiometry of the flame in each, as illustrated in Fig. 2.

Other variables such as spray distance and deposition rates (combination of feedrate and robot speed) were not considered at this stage of the study for coating deposition but recognized that they play an important role as well. However, the effect of feed rate, air flow in the combustion chamber, spray distance on particle state was monitored by diagnostic sensors.

Table 1 First-order process map: spraying parameters of Ni-20%Cr conditions

Condition	Gas flows				Normalized fuel/oxygen ratio ¹ λ^*	Total, lpm	Energy, kW	Substrate temperature, °C	Coating designation
	Fuel, lpm	Oxygen, lpm	Air, lpm	Fuel/oxy ratio λ					
1	50.9	207	351	0.18	0.78	621	69.6	200	A
2	60.2	198	351	0.22	0.96	621	82.3		
3	68.9	189	351	0.26	1.13	621	82.3		
4	76.9	181	351	0.30	1.30	621	80.6		
5	82.6	173	351	0.33	1.43	619	78.7	300	B
6	91.8	166	351	0.38	1.65	621	75.9		
7	54.3	225	316	0.19	0.83	607	74.2		
8	62.8	218	316	0.22	0.96	609	85.8	210	C
9	69.4	203	316	0.26	1.13	600	83.9		
10	77.9	196	316	0.30	1.30	602	81.6	260	D

¹Normalized fuel/oxygen ratios (λ^*) are shown with respect to the stoichiometric value (0.23), where $\lambda^* = \lambda / \lambda_{\text{stoich}}$. Nitrogen was used as carrier gas –12 lpm. DJ2700 HVOF System. Aircap: DJ2702. Spray distance 266 mm. Traverse spraying velocity 0.5 m/s. Feed rate: 23 g/min for coating deposition and splat collection, 9 g/min for diagnostics measurements. Supply pressure of gases in the console were kept constant at all times

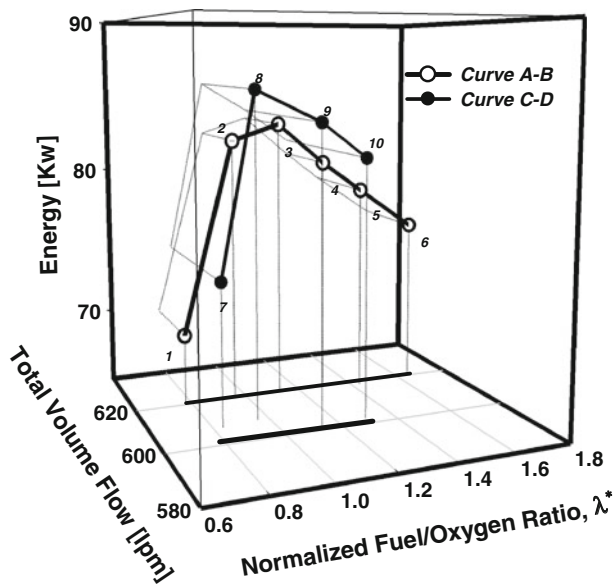


Fig. 2 Design of experiments, including two sets of parameters at different total volume flow and different gas ratios. Flame energy as a result of the combustion of the fuel is shown in the vertical axis

3.2 First-Order Process Maps: Spraying Parameters

Ni-20%Cr powder from Praxair Surface Technologies, Indianapolis, IN (particle size 5 to 45 μm), was used to spray coatings at a constant rate of 23 g/min. Powder was of spherical morphology with grain size of about 1-2 μm .

A water-cooled HVOF DJ2700 gun from Sulzer-Metco, Westbury, NY, with propylene as fuel was used in this study. Average values of temperature and velocity of the spray stream of different conditions were measured with a dual-fiber optical sensor device, Accuraspray G3 from Tecnar Automation LTEE, St-Bruno, QC, Canada.

From the design of experiments of a first-order process map (Fig. 2), four conditions were chosen to spray coatings denoted as A, B, C, and D, in Fig. 3—points (2), (6), (8), and (10), respectively, in Fig. 2. The coatings were deposited on plates onto the in situ coating property (ICP) sensor (Ref 17). Low-carbon steel plates of 230 mm length, 25.4 mm width and 1.6 mm thickness grit-blasted on both sides were used as substrates. Fifteen passes were sprayed in all experiments to produce coatings of around 0.3 mm thickness. Coatings of 1 mm thickness were also sprayed at these conditions to be used in indentation and thermal conductivity measurements.

Process diagnostics with Accuraspray were carried out at a relatively low feed rate of 9 g/min. The effect of flame quenching due to an increment in the feed rate was investigated on the curve-trend C-D. A feed rate of 23 g/min was used and similar spraying conditions (7)-(10) were sprayed and measured. Similarly, the effect of an increment in air flow fed to the gun was monitored incrementing 35 lpm in all the conditions in the case of the

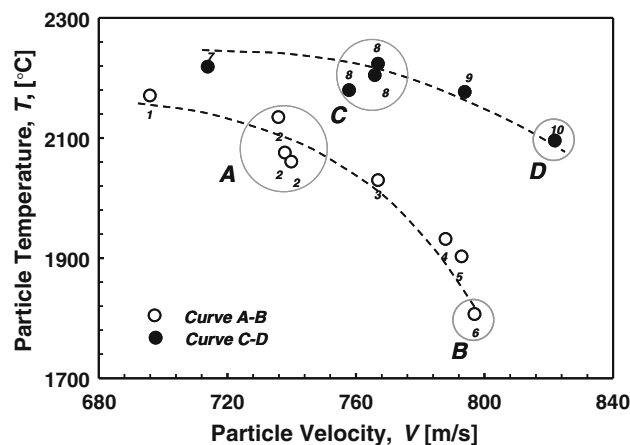


Fig. 3 First-order process map in a DJ-HVOF gun. From left to right, curves A-B and C-D represent particle states of Ni-20Cr particles sprayed at oxygen-rich towards fuel-rich conditions. Three measurements in random order at conditions (2) and (8) were done for repeatability control. Coatings for further characterization were sprayed at conditions denoted as A, B, C, and D

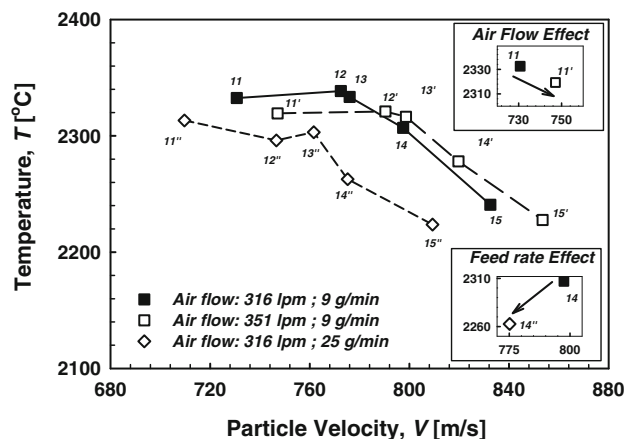


Fig. 4 Effect of air flow and feed rate increment on the particle state. Note conditions (11) to (15) correspond to conditions (7) to (10) of curve C-D in Fig. 3 after hardware renewal. Inset top right illustrates the magnitude of T-V change in particle state due to air flow increment for condition 11. Inset bottom right illustrates the same for condition 14 due to and increment in feed rate

regime represented in curve C-D. Results and trends are shown in Fig. 4.

Particle temperatures and velocities were also measured along the trajectory of the particles from 166 to 266 mm at every 25 mm increment. The gun was mounted on a six-axes robot (FANUC M-16i) which allowed for high-precision displacements without bias on control volume for diagnostics. Results are shown in Fig. 5.

3.3 Microstructural Examination

Coating cross-sections were examined by SEM (scanning electron microscope, Leo Zeiss 1550), at 2k \times magnification. Coatings were sectioned, mounted in epoxy,

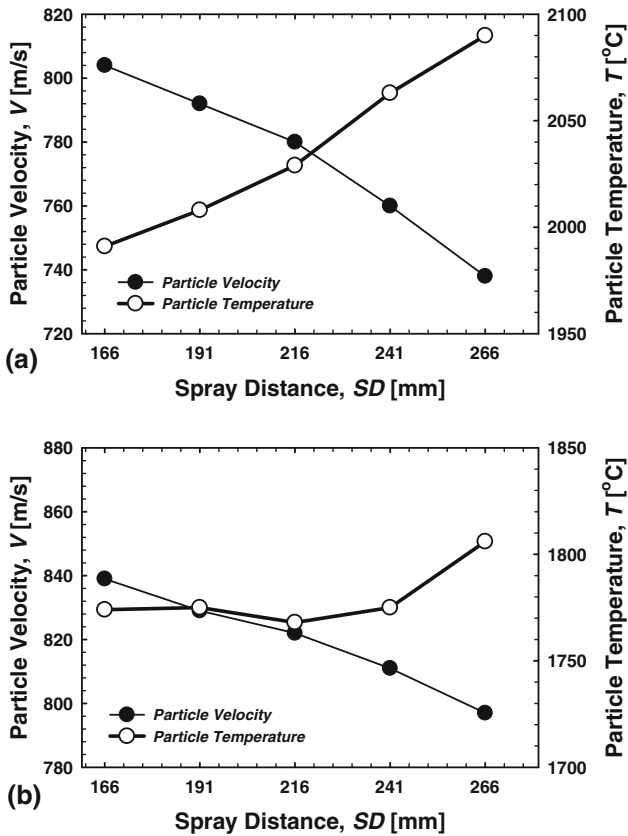


Fig. 5 Particle temperature and velocity for conditions A and B (respectively shown in plots (a) and (b)), at different spray distances. Spray distance for sprayed coatings is 266 mm

and polished to mirror finish up to 1 μm diamond suspension solution.

Splats were collected onto polished stainless steel substrates kept at room temperature. A shuttering system consisting of a window moved by a pneumatic arm in front of the particle stream was used to collect a snapshot of the in-flight particles. A splat map (at the same spraying feed rate of 23 g/min) was qualitatively characterized by SEM.

Phase analysis was investigated with x-ray diffraction and conducted on coatings and feedstock powder using $K\alpha$ Cu radiation ($\lambda = 1.54059$) at 40 kV and 25 mA in a SCINTAG/PAD-V instrument. EDAX (energy dispersive analysis) on SEM was also used to identify the oxide nature. Image analysis was performed on A, B, C and D samples to differentiate NiCr matrix from oxidation and other defects.

3.4 Stress Evolution and Residual Stress Measurements by ICP (In Situ Coating Property Sensor)

A Stony Brook developed in situ coating-property sensor (Ref 10) was used to monitor the curvature and temperature while spraying of four plates at the four spraying conditions A, B, C, and D. Substrate temperature is monitored via two contact thermocouples in the back of

the substrate. Considerations for calculation of stresses from the curvature measurements are explained elsewhere (Ref 10, 18) and summarized here. In HVOF, the intrinsic development of stress by each layer involves contributions from quenching of splats and peening on the deposited splats. The overall effect is defined in this paper as evolving stress.

Provided that each deposited pass is much thinner than the substrate, the stress developed by each layer is calculated by Stoney Formula (Ref 19) according to:

$$\sigma_{ev} = \frac{E'_s t_s^2}{6} \frac{d\kappa}{dt_c} \quad (\text{Eq 3})$$

where σ_{ev} is the evolving stress in the layer of dt_c thickness causing a $d\kappa$ curvature during deposition, t_s is the substrate thickness, and E'_s is the in-plane modulus of the substrate. $d\kappa/dt$ is usually taken after the first or second deposited passes because these layers usually are affected by interaction with the substrate. It is assumed that the change in stiffness of the substrate-coating system does not insert a significant error as new layers get deposited.

Thermal stress is calculated according to Brenner and Senderoff's formula (Ref 20) for thick coatings from the curvature change during cooling, using the modulus of the coating from the indentation result. The final residual stress value reported is the summation of the evolving stress plus the thermal stress.

4. Property Measurements

4.1 Thermal Conductivity Measurement

Thermal conductivity measurements were carried out on 12.5 mm diameter and 1 mm thick free-standing coating disks, coated with carbon, using Holometrix laser flash thermal diffusivity instrument. Measurements were made on two samples of each condition for nine times each.

4.2 Elastic Modulus Measurement

Microindentation testing was carried out on polished top-surfaces of thick coatings bonded to the substrates. Experiments were conducted in an instrumented indenter (Microtest 600, Micro-Materials Limited, Wrexham Technology Park, Wrexham, UK), using a WC-Co Berkovich indenter and an incremental load up to 5 newtons, at room temperature. Elastic modulus was calculated from the unloading portion (elastic recovery portion) of the load-depth records according to Oliver and Pharr method (Ref 21). Hardness was also extracted from this experiment.

4.3 Electrical Resistivity

Electrical resistivity was measured using a four-point probe (Model FPP-5000, Miller Design & Equipment) resistivity instrument. It consists of four equally spaced metal tips, with each tip supported by springs on the other end to minimize sample damage during probing.



High impedance direct current is provided during the measurement through the outer two probes and the voltage across the inner two probes is measured to determine the sample resistivity. Geometrical factors have to be considered due to the finite size and thickness of the specimen. In this work, the correction factors dependent on sample shape and dimensions were calculated based on the work of Topsoe (Ref 22) and Smiths (Ref 23). Measurements were made on one sample of each condition for nine times each in different orientations.

5. Results and Discussion

5.1 Synthesis of a First-Order Process Map

As mentioned earlier a first-order process map represents the relationship between gun parameters and the particle state. Such a map can be represented as a temperature-velocity space of the traveling particles with identification of specific operational regimes. Figure 3 represents a first-order process map of the present study of HVOF NiCr. Several important features are identified on this map.

A salient trend of particle temperature and velocity was observed when going from an oxygen-rich flame to a fuel-rich flame. Oxygen-rich chemistry conditions cause high temperature and low velocities of particles, and when tuning towards fuel-rich conditions, temperature decreases and velocity increases following a parabolic trend. The experiments carried out at higher total volume displaced the trend curves to lower temperature and velocity, which is understandable due to the lower energy input as computed in Eq 2. The energy level may also be affected by the nitrogen content from the air cooling down the flame to a higher extent in the set A-B compared to set C-D.

Analogous trends are observed in the projection of the curves of Fig. 2 on the plane of Energy-Normalized fuel/oxygen ratio in comparison with first-order process map in Fig. 3, which suggests that prediction of T-V particle condition can be exercised by flame energy computation. Except for the oxygen-rich conditions, higher energy flames define higher particle temperature at lower velocities, and otherwise. These trends have been found true for other materials, e.g., NiAl, Ni, WC-Co using DJ-2700 gun, and also other HVOF systems, i.e., JetKote (Deloro Stellite, Goshen, IN) torch with hydrogen fuel.

The energy computation of these oxygen-rich conditions assumes equilibrium combustion reactions that at the very fast reaction rate occurring inside the nozzle may under predict the energy input at this condition. Gas input enthalpies and dissociation of not only fuel (C_3H_6) but other species like CO_2 and H_2O also contribute to the energy of the flame and are not considered here. The values proposed here are not intended to be exact, but a relative framework to identify the kinetic and thermal energy transferred to the particles. In spite of these limitations, when comparing conditions of fixed fuel/oxygen ratios with different energy levels (in Fig. 3, comparing

conditions 1 to 7, 2 to 8, 3 to 9 and 4 to 10), it is still observed that higher energy levels in the flame yield higher kinetic and thermal energies in the particles according to the principle of conservation of energy. Percentile differences in T-V (i.e. between 2 and 8, 3 and 9) are more significant than in energy levels, and both, measurements and calculations have intrinsic errors; however, the correlation remains.

An independent increment of air flow to the flame results in decrease of the temperature and increase of the speed of the particles, as in Fig. 4. This suggests that the main effect of the air flow was not to increase the energy input by adding extra-oxygen to the flame but to increase the drag force to the particles and shorten their dwell time, as well as to cool down the flame. The magnitude of the temperature and velocity change is relatively small (see top-right inset of Fig. 4) in comparison to what can be achieved by tuning the fuel-oxygen mixture. Feed rate was also found to play a role in the temperature and velocity of the ensemble of particles. The typical flame quenching effect was observed when increasing the flow rate from 9 to 25 g/min. The parabolic trends in the T-V space were found not to be susceptible to change to either linear increment of air flow or flame quenching.

5.1.1 Particle State Monitoring Along the Axial Trajectory. Particles accelerate within the divergent section of nozzle and the first ~100 mm outside the nozzle (Ref 15). Afterwards, the gas-flame decreases in velocity and temperature and simultaneously, more and more retarding force acts on the particles due to air entrainment. For this reason, particles decelerate at longer spray distances as observed in conditions A, B in Fig. 5.

The plume jet core changes substantially from oxygen-rich to fuel-rich conditions. The differences in the flame are observable to the naked eye: oxygen-rich flames look bluish and short, whereas fuel-rich flames are yellowish and long. It is hypothesized that the higher amount of fuel extends the combustion to the outside of the nozzle. As a result, longer flames are observed. It is expected that longer flames reduce the resistance of the surrounding air due to the low density of the gases at high temperature. For this reason, particles decelerate less in B condition compared with A for the same trajectory.

The temperature trends are also notable. Temperature was found to increase as the particles fly away from the nozzle. Although particles find a colder atmosphere as they travel, the oxidation is enhanced in this downstream region due to extensive air entrainment within the combustion flow field.

The enthalpy of the exothermic reaction of formation of chrome oxides, Cr_2O_3 is around -1.14×10^3 kJ/mol (Ref 24), and can input sufficient heat as to increase temperature in the depleted NiCr of the particle. Moreover, measurements are consistent with the fact that a longer flame (B) would protect the particle from oxidation by means of shortening the interaction with the surroundings downstream of the flame. This is enhanced by the fuel burning the oxygen within the flame upstream. As a result, B condition shows a small increment in particle temperature and only at the deposition distance (266 mm)

where the flame is essentially extinguished. The microscopy analysis indicates highest oxidation of particles sprayed at stoichiometric conditions whereas fuel-rich conditions (longer flames) show less oxidation. In summary, the oxide content of the microstructure will respond to this shielding effect of a longer flame (reduced air entrainment), the chemistry of the flame, and the particle temperature.

It is noted that scanning the temperature drop or increment along the spray stream may be a useful tool (when the oxide formation is an exothermic reaction in the feedstock) to optimize the torch parameters with respect to designing coatings with appropriate oxide content. Similar results were observed by Lih et al. (Ref 6) when spraying CrC on a matrix of NiCr and Lugscheider et al. (Ref 2) spraying NiCoCrAlY.

It is also hypothesized that the emission readings of Accuraspray system may be biased by the formation of oxides on the outer shell of the in-flight particles. Decoupling the effect of exothermic reactions and emissions from the newly formed oxide are beyond the scope of this paper. Further research on T-V evaluation of individual particles could possibly discriminate any bias produced by the ensemble measurement of the Accuraspray system.

5.2 Microstructure Characterization

Figure 6 shows the cross-sectional microstructures of the various deposits. Overall coatings show high density

and almost no porosity. Coalescence of intersplat boundaries is expected to be containing metallurgical bonding owing to the high temperature of the particles. However, the presence of interlamellar oxide can also modify intersplat interfaces. The image analysis results, including oxides and porosities, are the following: $A = 12.8\%$; $B = 6.5\%$, $C = 16.4\%$, $D = 9.3\%$.

Significant differences are observed in the four cases. (i) A and C conditions (Fig. 6a, c) show a lamellar structure with almost no interlamellar porosity but oxides. A structure of thin flattened splats can be observed. Relatively longer residence times in the flame due to the lower velocities of particles at A and C conditions resulted in greater oxidation. C condition being of higher particle temperature shows slightly higher oxide content than A condition. (ii) B condition (Fig. 6b) shows a lumpy microstructure due to lack of liquid flow because of the low particle temperature. Very few globular pores are observed and no interlamellar pores are present. Oxidation on the splat is very low owing to the shorter residence time and the shielding effect of the reducing flame. (iii) D condition (Fig. 6d) shows combined attributes of A-C with B features. Although D condition experienced the shorter residence time, it clearly experienced a larger heat input in the flame compared to B condition which promoted the oxidation of the particles.

Oxidation after deposition has also been reported due to the heat input from the flame (Ref 5, 7). Substrate temperature monitoring via ICP sensor (Fig. 8a-b and c-d; and Table 1) yielded values between 200 to 300 °C, being

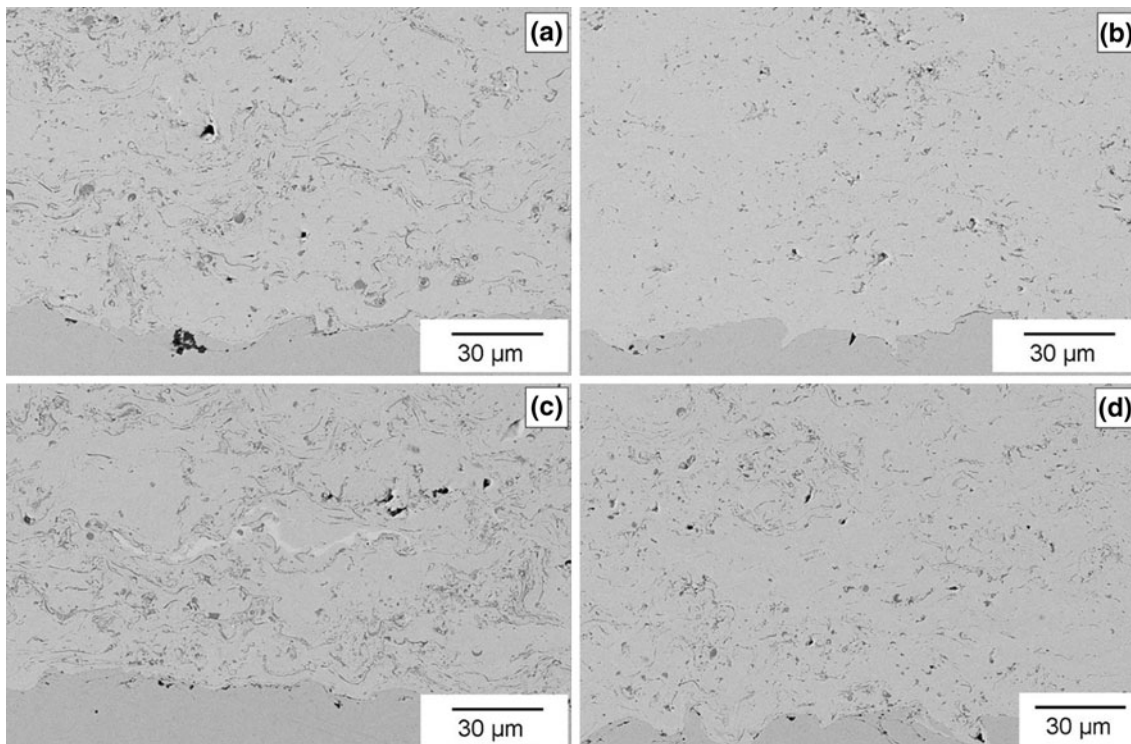


Fig. 6 SEM images (2k \times) of four Ni-20Cr coatings sprayed at different particle state conditions shown in Fig. 3 (i.e. SEM image (a) corresponds to condition A in Fig. 3, etc.)

the higher for the longer flames of fuel-rich conditions, B and D. These temperatures are relatively low to promote oxidation, the values are within a short range to represent significant differences among the coatings, and moreover, their possible effect does not concur with the microstructure, i.e. highest substrate temperature 300 °C in condition B shows the lowest oxidation. Therefore, the oxidation effect after deposition is considered secondary in these coatings.

Literature has reported the presence of NiO, NiCr₂O₄, Cr₂O₃ (the latter, after heat treatment only) as the oxide present when spraying Ni-Cr (Ref 1, 7). On the other hand, Sidhu et al. (Ref 8, 25) have reported that Cr₂O₃ is

prone to form during the spraying of Ni-20Cr wired feedstock by HVOF. In the present study, EDAX has suggested that the oxide present in the as-sprayed coating shows high content of Cr and it is probably Cr₂O₃. XRD diffraction patterns did not identify diffraction peaks of chrome oxides, probably due to the low content of the oxide, texture in the coatings, and/or roughness effects.

5.2.1 Splats-splat maps. Splats represent the building blocks of a thermal spray coating and as such provide an excellent visual representation of the processing effects. Splats were synthesized at the four identified process conditions (A, B, C and D) and are shown in Fig. 7a, b, c and d, respectively. All the samples showed an assortment

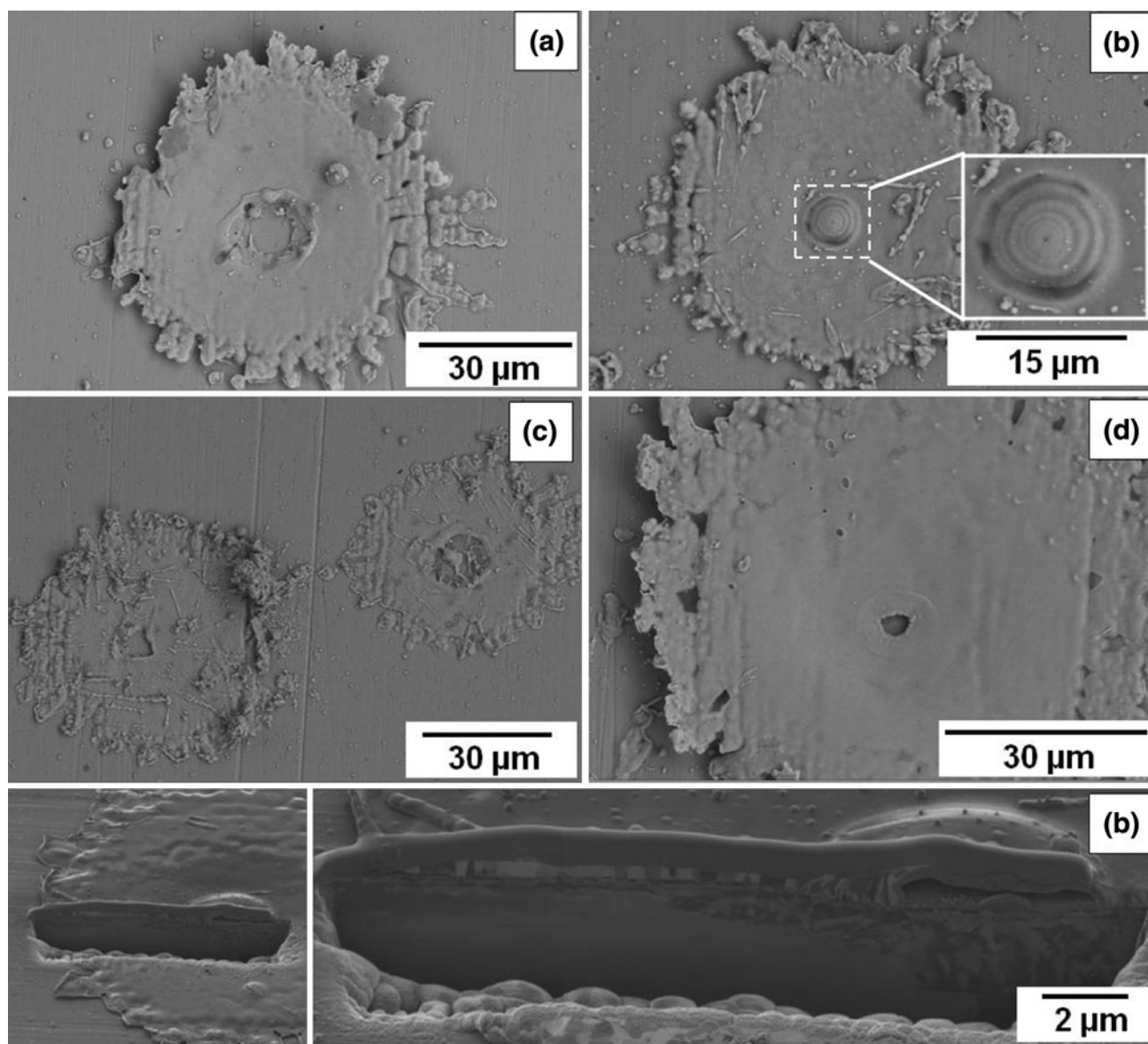


Fig. 7 Individual splats collected from the four different conditions, named A, B, C and D in Fig. 3. SEM image labels correspond to the same named conditions in Fig. 3. Splats of conditions A, C, and D show craters in the center point due to release of gas trapped during impact. Image (b) (right upper corner) shows a typical splat of condition B where gas was trapped during impact. Inset shows magnifications of the dome formed on top of gas pocket. At the bottom, a cross-section FIB of a splat sprayed under condition B is showing the gas pocket trapped during spreading

of molten and partially molten particles in the center-populated and scattered areas.

By analyzing scattered splats, some discrimination can be made about their in-flight history and deposit formation dynamics. It was found that smaller particles suffer more oxidation in conditions of high-particle temperature, such as in A and C conditions, whereas in B condition, particles of the same scale-size are not as oxidized. This is in agreement with the microstructural features reported in the cross sections. In terms of morphology, Fig. 7 also illustrates typical splats of different melting states. In A, C, and D conditions, the air pocket that usually gets trapped when spraying molten particles at high velocity (Ref 26) was freed after the spreading of splat, but in B, the higher viscosity due to a lower melting state retains the air pocket as observed in the FIB (focused ion beam) cross section of the dome. Columnar grain growth can be observed in the dome that trapped the air. It should be noted that splats from all conditions show much smaller grain size than the original particle grain size seen in the feedstock, which is an indicator of the full melting state of the particles when the impact occurred.

5.3 Evolution of Stresses and Residual Stress

Plots of temperature versus time and curvature versus time for sprayed conditions are presented in Fig. 8. Conditions B and D reached high-surface deposition temperature even though the particle temperature was not the highest. This is because a more reducing condition (high-fuel content) elongates the flame and thus the temperature field producing a hotter substrate temperature. This did not show notable effects on the oxidation of the deposited splats, for instance: B condition shows the lowest oxide content at the highest substrate temperature, which indicates that the oxide content of the coatings is predominantly determined by the in-flight reactions. Furthermore, this high substrate temperature defines a larger cooling gradient to room temperature which imposes more tensile stress due to thermal contraction.

Upon analyzing curvature curves, in all conditions in the first pass, quenching stresses prevail due to limited plastic deformation of the steel substrate. Subsequently, each pass contributes to input compressive stresses owing to the peening effect on the deposited NiCr. Particles with higher velocity contribute with more intensity to buildup compressive stresses as can be seen comparing the slopes of the curvature curves during spraying. At higher substrate temperature, a reduced effect of peening is expected provided that materials yield at lower stress values at higher temperatures. However, this trend is not observed among these coatings probably because temperature differences are not as significant as to show peening reduction.

The stresses in the coatings at the end of the deposition stage are all compressive with higher values for conditions B and D, as observed in Fig. 9. These two conditions also present higher substrate temperatures and as a result thermal stresses are also higher due to the larger thermal

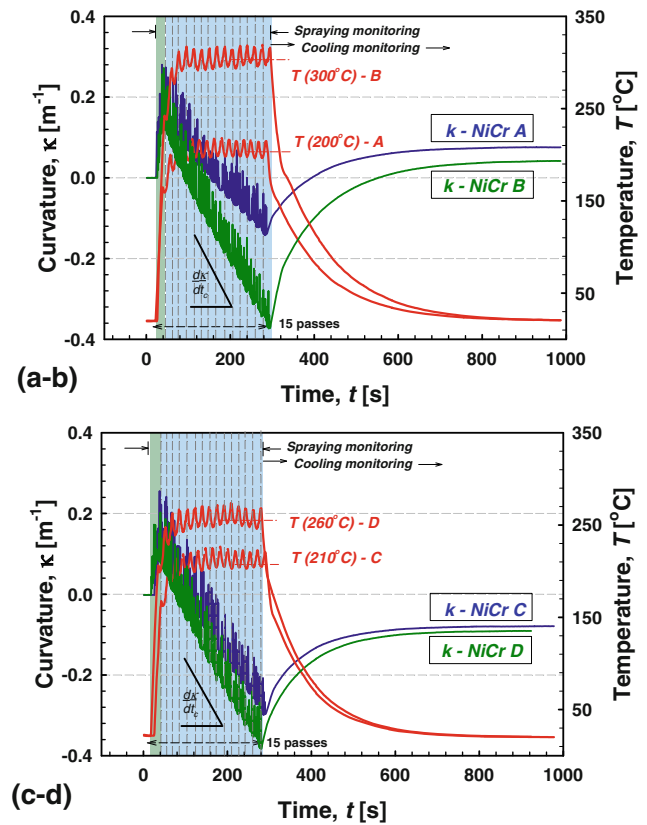


Fig. 8 Curvature and temperature evolution during spraying (shaded region) and cooling of NiCr coatings. Evolving stress is evaluated considering the slope of the curvature curves during the spraying stage. (a-b) shows the data corresponding to conditions A and B in Fig. 3 and (c-d) to conditions C and D

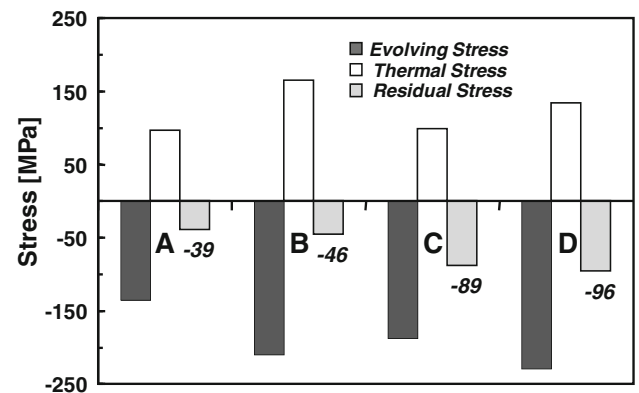


Fig. 9 Stress developed during deposition (evolving stress), during cooling (thermal mismatch) and after cooling (residual stress) for coatings deposited under A, B, C, D conditions

gradient from the average deposition temperature to room temperature.

The final residual stress of coatings is a combination of the stress developed during deposition (dependent on particle state, substrate temperature, others) and the

thermal stresses (dependent on the coefficients of thermal expansion, temperature gradients, coating/substrate stiffness). Particularities of the combinations of these two are only enabled during the monitoring in situ of the stress evolution. For instance, in Fig. 8, A and B conditions are of quite different particle state but both end in similar curvature, but different residual stress state as seen in Fig. 9. In Fig. 8 and 9, D condition shows higher peening intensity and also higher thermal stress, so the final curvatures for C and D conditions are coincidentally in compression at similar stress value.

5.4 Property Evaluation

5.4.1 Thermal Conductivity. In Ref 27, it was found that thermal conductivity (κ) of Ni-5%Al by different thermal spray processes is enhanced by a combination of high kinetic energy and high thermal energy of the particles. As a result, HVOF coatings showed highest thermal conductivity among air plasma, arc spray and cold spray processes. Thus, it is expected that improved interaction of the interlayer/intersplat interfaces by intimate contact or metallurgical bonding will result in high thermal conductivity. Expanding on this principle, in Fig. 10, it can be observed that the condition of high kinetic energy (enhancing compaction) and high thermal energy (enhancing wetting and metallurgical bonding) show the highest thermal conductivity (D condition). Besides, the high substrate temperature during spraying, observed in Table 1 improved the cohesion of the particles. At lower velocity and high temperature (A, C conditions), the presence of oxide on the interface drives the thermal conduction lower. An increase in the oxide content decreases the thermal conductivity of the composite provided that the conductivity of the oxide is lower than that of the alloy (APS Cr_2O_3 coating, $k = 2.8 \text{ W/mK}$ (Ref 28); densified Cr_2O_3 coating, $k = 3.7 \text{ W/mK}$ (Ref 29)).

5.4.2 Electrical Resistivity. Similarly to the thermal conductivity, the electrical resistivity (ρ) of thermal spray coatings responds to the true contact between splats and the content of oxide and defects present in the

microstructure (Ref 30). The lowest thermal and electrical resistivity was measured in B and D conditions, owing to the low oxide content and high intimate contact between splats. However, the highest ρ was observed in A but not in C condition (as expected from the thermal conductivity measurement) probably due to a higher dependency of ρ to the metallurgical bond (obtained at higher particle temperature in C condition) and not to the oxide content. It should be noted that κ -measurements were carried out through the thickness of the microstructure, whereas the ρ -measurements were in-plane measurements. The anisotropy of ρ in-plane versus through thickness was found to be negligible for HVOF Ni-5Al coatings ($\rho_{\text{in-plane}}/\rho_{\text{through thickness}} = 1.1$) by Sharma et al. (Ref 30), so it is considered that the trends of thermal and electrical resistivity are comparable.

5.4.3 Indentation Elastic Modulus. Elastic modulus for thermal spray coatings provides a quantitative descriptor of the consolidated integrity of the splat-based assemblage. It combines the typical elastic response of splat material (alloy and oxide) and the bonded interfaces. In this study, indentations sampled a reasonable volume of material (including a number of splats and interfaces) so as to cross compare the consolidated elastic behavior of the coatings incorporating all microstructural effects. In Fig. 11, the condition of low oxide content—B condition (high velocity, low temperature)—shows the highest elastic modulus owing to the presence of less depleted Ni-20Cr alloy with good intersplat bonding, as discussed in Fig. 10. D-condition, although of the highest intersplat bonding, as it shows oxidation its elastic modulus decreases. Similarly, as the NiCr alloy loses Cr to the oxide, and the latter affects the interfaces, elastic modulus decreases in A- and C-conditions. In conclusion, the highest elastic modulus can be obtained by spraying conditions of high velocity and low temperature. However, in practice one should be careful since these kind of conditions may fall in the regime of unmelted particles.

5.4.4 Hardness and Evolving Stress. The hardness in high-velocity sprayed coatings responds to the strain hardening caused by the peening effect, here represented

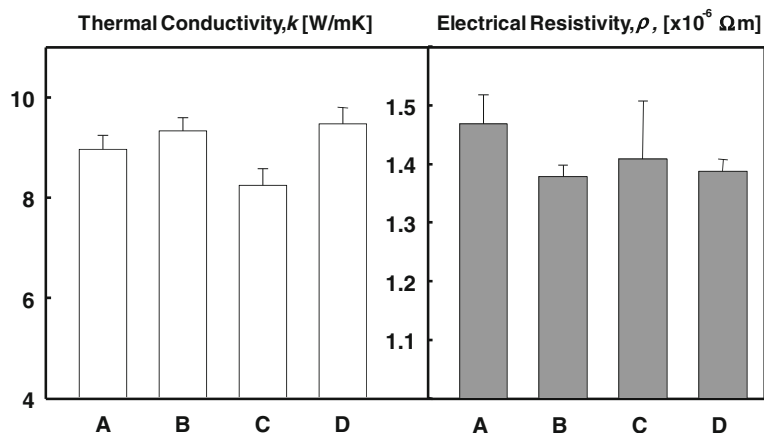


Fig. 10 Thermal conductivity and electrical resistivity of coatings deposited under A, B, C, D conditions

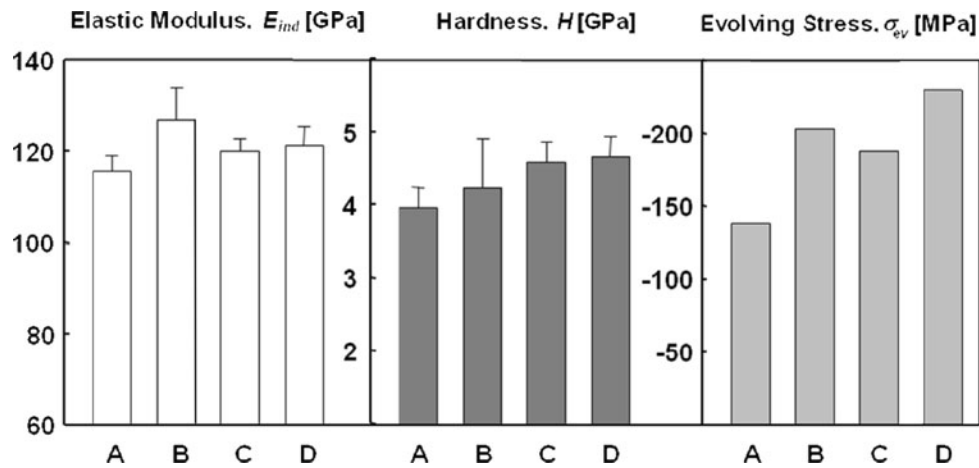


Fig. 11 Elastic modulus, hardness and evolving stress for coatings deposited under A, B, C, D conditions

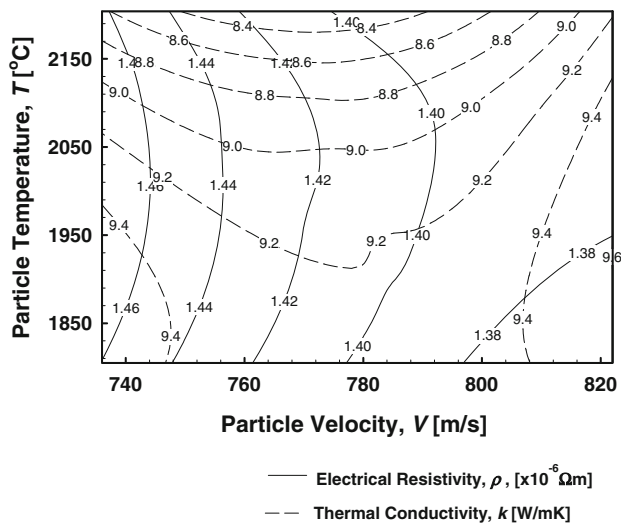


Fig. 12 Second-order process maps: thermal conductivity and electrical resistivity of Ni-20Cr coatings by HVOF-DJ-2700 system

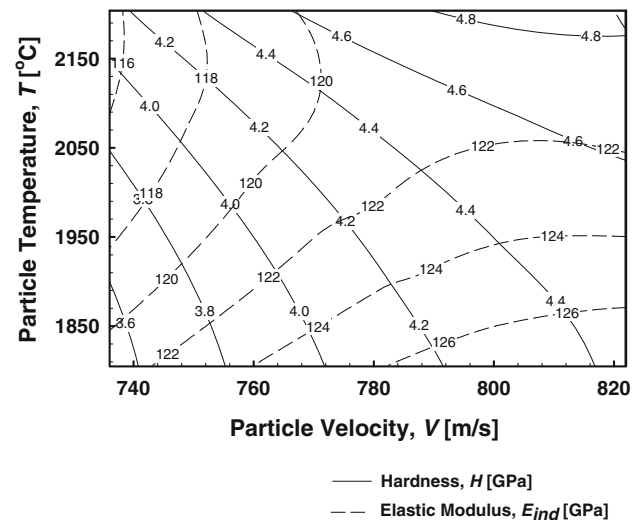


Fig. 13 Second-order process maps: elastic modulus and hardness of Ni-20Cr coatings by HVOF-DJ-2700 system

by compressive evolving stress. The effect of residual stress is not discussed here considering the relative low magnitude with respect to the plastic deformation during the indentation. In Fig. 11, the trend of higher particle momentum to higher induced compressive stresses in the microstructure is observed. The slope of the curves of curvature versus time during deposition in Fig. 8 reflects the intensity of the peening of the impacting particles. Figure 11 almost reflects a similar trend for hardness, except that C is slightly harder than B, owing to the presence of more oxide in C. The mechanical behavior of these coatings (hardness, elastic modulus, evolving stress) was found to be closely related to the intensity of impact of the particles. Therefore, the monitoring of particle velocity can be directly correlated to stiffness and hardness (higher velocity, higher hardness, higher modulus), except for condition C in which the particle temperature

may have played a more dominant role in the evolution of the microstructure due to oxidation.

5.5 Second-Order Process Maps

Through thickness thermal conductivity, and in-plane electrical resistivity, as well as through thickness indentation modulus and hardness are plotted as contour plots in the T - V space in Fig. 12 and 13, respectively. Due to the availability of a few numbers of points, these contour plots are meant only illustrative of the methodology of process maps. The purpose of these second-order process maps is to provide a tool for designer to choose coatings of selected combination of properties and specify the values of T - V of the particle state. For that condition, actual operational parameters are specified from the first-order map.

Table 2 Range of properties values of NiCr coatings sprayed at different spraying conditions

Property	Prop/bulk prop	Property measurements, \pm SD				Variability (max-min)/bulk, %	SD variability (aver SD/bulk), %
		A	B	C	D		
Thermal conductivity, W/mK	0.50-0.58	8.96 \pm 0.28	9.32 \pm 0.27	8.25 \pm 0.29	9.47 \pm 0.33	7.4	1.8
Electrical resistivity, $\mu\Omega \cdot m$	1.28-1.36	1.47 \pm 0.05	1.38 \pm 0.02	1.41 \pm 0.10	1.39 \pm 0.02	8.3	4.4
Elastic modulus, GPa	0.56-0.62	115.7 \pm 3.4	126.9 \pm 7.3	119.9 \pm 3.1	121.1 \pm 4.4	5.5	2.2
Hardness, GPa	1.37-1.61	3.9 \pm 0.3	4.2 \pm 0.7	4.6 \pm 0.3	4.7 \pm 0.3	24.2	13.4

Note: Property values, standard deviations, and coating property/bulk property ratios are presented. Individual measurements of thermal conductivity, elastic modulus, electrical resistivity and hardness correspond to the second-order process maps of Fig. 12 and 13
Bulk properties: Thermal conductivity: 16.4 W/mK (Ref 31); elastic modulus: 215 GPa (Ref 29); electrical resistivity: 1.08 $\mu\Omega \cdot m$ (Ref 32); hardness: 2.5-2.9 GPa (Ref 29)

5.6 Property Variability

Researchers and engineers are all interested in the process induced variability in property values that any material-processing system performs. Whether they are seeking for a broad range of variability or trying to minimize the process effect on resulting properties, the triad process-microstructure-property relationship has to be carefully established. In the present study, this relationship for a DJ system spraying NiCr powder can be discussed. In Table 2, property values as well as standard deviations of measurements are presented. The overall property variability is relatively tight (<10%), except for the hardness measurements, which is shown to be very sensitive to the peening intensity.

It is also observed in Table 2 that the properties are lower with respect to the bulk values for thermal/electrical conductivity (where electrical conductivity = $1/\rho$) and modulus due to the presence of intersplat interface and oxides, but higher for hardness owing to strain hardening. Also, the standard deviation of measurements (i.e. modulus and hardness for coating B) indicates the degree of heterogeneity of the microstructures when testing different areas of the samples. It is noted that although the differences between property values may fall within their standard deviation for two different coatings the variability of the standard deviation is smaller compared to the range of property variability. The latter assures the differences are real statistically.

6. Conclusions

Combination of microstructural characterization, such as micrographs, splat collection, complement the understanding of particle state, oxidation levels, flattening ratios, and pores-cracks architecture of the coating.

Process Maps were used in the present study to examine the effect of spraying parameters on the formation, microstructure and properties of Ni-20%Cr coatings by HVOF on a DJ-System. Concurrent analysis of melting state, oxide content of splats and microstructures and properties proved that HVOF formation of coatings is sensitive to changes in particle state.

Careful manipulation of the spraying parameters allowed us to build a first-order process map (a T-V diagram), in which the characteristics of the flame could be correlated to the particle state (temperature, velocity) and the substrate temperature. The results suggest a correlation between flame energy and particle temperature, and flame chemistry (fuel/oxygen ratio) and particle velocity. Thus, when spraying with flames richer in fuel, the particle velocity increases and as the flame energy decreases, the temperature also decreases. These two variables (flame energy and fuel/oxygen ratio) would allow the operator to explore the T-V diagram at discretion. It is noted that an exact computation of flame energy may not be trivial considering the changes in combustion rates, gas dynamics, chamber pressures and cooling effects from the air when using different spray parameters. The approach presented here is a first approximation, but the treatment of process variables (varying fuel/oxygen ratio, fixing total flow and air flow) allows for a consistent method to explore the T-V space.

The monitoring of T-V along the spray stream-downstream showed that the exothermic reaction of formation of the oxide inputs heat during flight. Particles get hotter as they travel away from the core of the flame due to the interaction with the air (oxygen) entrained. In fuel-rich conditions, some oxygen of the surrounding gets consumed by the fuel that did not burn effectively in the plume upstream. As a result, particles are sprayed through an ambient with low oxygen content resulting in lower oxidation.

Property evaluation for second-order process maps revealed the following trends.

To enhance thermal conductivity, high kinetic energy with high thermal energy of particles is required as to deposit dense coatings with improved intersplat bonding (metallurgical, intimate mechanical contact); as long as the oxide content is relatively low as to avoid affecting the interfaces seriously.

Electrical resistivity responds similarly to thermal transport with lower values at high thermal-kinetic energy of the particles. Its response to oxide content is probably less important providing an electron path exists in the splat/splat interfaces.

Stiffer coatings resulted at high particle speed and low melting state.

Differences in particle state also reflected different evolution of stress buildup during spraying in the coatings. Higher induction of compressive stresses due to peening was identified at higher particle velocities.

It is highlighted that the monitoring of the stress developed during spraying can depict notably differences in the actual formation of the coating at different particle states. Evolving stress and substrate temperature are key factors when considering strain hardening of the coating, compaction, and residual stress development.

Although microstructures of coatings were dissimilar, such feature differences were not significantly representative in property values. The maximum difference in property values among the tested coatings is less than 8.3% for electrical resistivity, 7.4% for thermal conductivity, and 5.5% for elastic modulus (percentages are higher than the resolution of the measuring techniques). Hardness was the more process sensitive property, showing the maximum range of property variability 24.2%. This validates the industrial practice of hardness evaluation to benchmark coatings. Further research should clarify whether these differences among these coatings are substantial when subjecting the coatings to in-service conditions or whether the material/processing window in this study represents a “forgivable” variability.

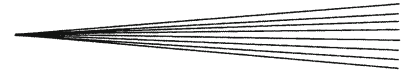
The *Process Map* methodology constitutes an excellent tool towards addressing the effects of spraying parameters in production of coatings. The applicability of the method is universal for any thermal spray technology. In this regard, the present results constitute a guideline to explore other HVOF-systems and materials (i.e. cermets: WC-Co, CrC-NiCr, etc.).

Acknowledgments

This research was supported by the GOALI-FRG program of the National Science Foundation under award number CMMI 0605704 and by the Consortium of Thermal Spray Technology at the Center for Thermal Spray Research in Stony Brook University. The authors would like to thank Prof. Margaret Hyland and Anh Tran for the FIB micrographs.

References

- R. Knight and R.W. Smith, HVOF Sprayed 80/20 NiCr Coatings—Process Influence Trends, *Proceedings of the International Thermal Spraying Conference & Exposition*, C.C. Berndt, Ed., ASM International, 1993, p 159-164
- E. Lugscheider, C. Herbst, and L. Zhao, Parameter Studies on High-Velocity Oxy-Fuel Spraying of MCrAlY Coatings, *Surf. Coat. Technol.*, 1998, **108-109**(1-3), p 16-23
- E. Turunen, T. Varis, T.E. Gustafsson, J. Keskinen, T. Falt, and S.-P. Hannula, Parameter Optimization of HVOF Sprayed Nanostructured Alumina and Alumina-Nickel Composite Coatings, *Surf. Coat. Technol.*, 2006, **200**(16-17), p 4987-4994
- E. Turunen, T. Varis, S.-P. Hannula, A. Vaidya, A. Kulkarni, J. Gutleberg, S. Sampath, and H. Herman, On the Role of Particle State and Deposition Procedure on Mechanical, Tribological and Dielectric Response of High Velocity Oxy-Fuel Sprayed Alumina Coatings, *Mater. Sci. Eng. A*, 2005, **415**(1-2), p 1-11
- J.A. Hearley, J. Little, and A.J. Sturgeon, The Effect of Spray Parameters on the Properties of High Velocity Oxy-Fuel NiAl Intermetallic Coatings, *Surf. Coat. Technol.*, 2000, **123**(2-3), p 210-218
- W.-C. Lih, S.H. Yang, C.Y. Su, S.C. Huang, I.C. Hsu, and M.S. Leu, Effects of Process Parameters on Molten Particle Speed and Surface Temperature and the Properties of HVOF CrC/NiCr Coatings, *Surf. Coat. Technol.*, 2000, **133-134**, p 54-60
- J. Saaedi, T.W. Coyle, S. Mirdamadi, H. Arabi, and J. Mostaghimi, Phase Formation in a Ni-50Cr HVOF Coating, *Surf. Coat. Technol.*, 2008, **202**(24), p 5804-5811
- T.S. Sidhu, S. Prakash, and R.D. Agrawal, Hot Corrosion Performance of a NiCr Coated Ni-Based Alloy, *Scr. Mater.*, 2006, **55**(2), p 179-182
- F. Tang, L. Ajdelsztajn, and J.M. Schoenung, Characterization of Oxide Scales Formed on HVOF NiCrAlY Coatings with Various Oxygen Contents Introduced During Thermal Spraying, *Scr. Mater.*, 2004, **51**(1), p 25-29
- J. Matejcek and S. Sampath, In Situ Measurement of Residual Stresses and Elastic Moduli in Thermal Sprayed Coatings: Part I: Apparatus and Analysis, *Acta Mater.*, 2003, **51**(3), p 863-872
- S. Sampath, X. Jiang, A. Kulkarni, J. Matejcek, D.L. Gilmore, and R.A. Neiser, Development of Process Maps for Plasma Spray: Case Study for Molybdenum, *Mater. Sci. Eng. A*, 2003, **348**(1-2), p 54-66
- A. Vaidya, V. Srinivasan, T. Streibl, M. Friis, W. Chi, and S. Sampath, Process Maps for Plasma Spraying of Yttria-Stabilized Zirconia: An Integrated Approach to Design Optimization and Reliability, *Mater. Sci. Eng. A*, 2008, **497**(1-2), p 239-253
- M. Friis and C. Persson, Control of Thermal Spray Processes by Means of Process Maps and Process Windows, *J. Therm. Spray Technol.*, 2003, **12**(1), p 44-52
- W. Rusch, Comparison of Operating Characteristics for Gas and Liquid Fuel HVOF Torches, *Thermal Spray 2007: Global Coating Solutions*, ASM International, May 14-16, 2007 (Beijing, China), ASM International, 2007, p 572
- M. Li and P.D. Christofides, Multi-Scale Modeling and Analysis of an Industrial HVOF Thermal Spray Process, *Chem. Eng. Sci.*, 2005, **60**(13), p 3649-3669
- V. Faires, *Thermodynamics*, 3rd ed., The MacMillan Company, 1957
- S. Sampath and J. Matejcek, Method and Apparatus for Determining Process-Induced Stresses and Modulus of Coatings by In-Situ Measurement, US Patent 6478875
- S. Kuroda, Y. Tashiro, H. Yumoto, S. Taira, and H. Fukanuma, Peening Action and Residual Stresses in HVOF Thermal Spraying of 316L Stainless Steel, *15th International Thermal Spray Conference*, Vol 1, 1998, p 569-574
- G.G. Stoney, The Tension of Metallic Films Deposited by Electrolysis, *Proceedings of the Royal Society*, Vol A82, London, 1909, p 172-175
- A. Brenner and S. Senderoff, Calculation of Stress in Electrodeposits from the Curvature of a Plated Strip, *J. Res. Natl. Bur. Stand.*, 1949, **42**(105), p 105-123
- W.C. Oliver and G.M. Pharr, An Improved Technique for Determining Hardness and Elastic-Modulus Using Load and Displacement Sensing Indentation Experiments, *J. Mater. Res.*, 1992, **7**(6), p 1564-1583
- H. Topsoe, Geometric Factors in Four Point Resistivity Measurement, Bridge Technology, 1968
- F.M. Smiths, Measurement of Sheet Resistivities with the 4-Point Probe, *Bell System Techn. J.*, 1958, p 711-718
- A.D. Mah, Heats of Formation of Chromium Oxide and Cadmium Oxide from Combustion Calorimetry, *J. Am. Chem. Soc.*, 1954, **76**(13), p 3363-3365
- T.S. Sidhu, S. Prakash, and R.D. Agrawal, Characterisation of NiCr Wire Coatings on Ni- and Fe-Based Superalloys by the HVOF Process, *Surf. Coat. Technol.*, 2006, **200**(18-19), p 5542-5549
- L. Li, B. Kharas, H. Zhang, and S. Sampath, Suppression of Crystallization During High Velocity Impact Quenching of Alumina Droplets: Observations and Characterization, *Mater. Sci. Eng. A*, 2007, **456**(1-2), p 35-42



27. S. Sampath, X.Y. Jiang, J. Matejcek, L. Prchlik, A. Kulkarni, and A. Vaidya, Role of Thermal Spray Processing Method on the Microstructure, Residual Stress and Properties of Coatings: An Integrated Study for Ni-5wt.%Al Bond Coats, *Mater. Sci. Eng. A*, 2004, **364**(1-2), p 216-231
28. N. Spinicchia, G. Angella, R. Benocci, A. Bruschi, A. Cremona, G. Gittini, A. Nardone, E. Signorelli, and E. Vassallo, Study of Plasma Sprayed Ceramic Coatings for High Power Density Microwave Loads, *Surf. Coat. Technol.*, 2005, **200**(1-4), p 1151-1154
29. Properties and Selection: Nonferrous Alloys and Special-Purpose Materials, *Metals Handbook*, 10th ed., H.C. ASM International, 1990
30. A. Sharma, R. Gambino, and S. Sampath, Anisotropic Electrical Properties in Thermal Spray Metallic Coatings, *Acta Mater.*, 2006, **54**(1), p 59-65
31. T. Yoshihiro, O. Kenji, M. Tetsuo, and S. Tomoo, Thermal Conductivity in Nickel Solid Solutions, *J. Appl. Phys.*, 1997, **81**(5), p 2263-2268
32. A.A. Al-Aql, Electrical Resistivity Measurements in Ni-Cr Alloys, *Mater. Des.*, 2003, **24**, p 547-550